A simple way to use X-ray micro-tomography to infer elastic properties of heterogeneous materials: application to sedimentary rocks

Title: A simple way to use X-ray micro-tomography to infer elastic properties of heterogeneous materials: Application to sedimentary rocks

Authors: Pierre-Louis Valdenaire[1†], Jonathan Perrin[2], Olivier Grauby[3], Franz-Josef Ulm[4], Roland J. M. Pellenq[1,4]

Authors affiliations:

[1]*MultiScale Material Science for Energy and Environment, MIT-CNRS-Aix-Marseille Université Joint Laboratory, Massachusetts Institute of Technology, Cambridge, MA 02139, USA*

[2]*Division expériences, Synchrotron Soleil, 91192 Gif-sur-Yvette, France*

[3]*Aix-Marseille Université, CNRS-UMR 7325 CINaM (Centre Interdisciplinaire de Nanoscience de Marseille), Campus de Luminy, 13288 Marseille cedex 9, France*

[4]*Department of Civil and Environmental Engineering, Massachusetts Institute of Technology, Cambridge, MA 02139, USA*

†corresponding author: Pierre-Louis Valdenaire, MultiScale Material Science for Energy and Environment, MIT-CNRS-Aix-Marseille Université Joint Laboratory, Massachusetts Institute of Technology, 400 Main street, E19-722, Cambridge, MA 02139, USA. Phone: 617-324-4357 Email: plvalden@mit.edu

ABSTRACT

Macroscopic mechanical properties of materials depend directly on their microstructure. Microscopy, and more specifically tomography, is a key method for studying microstructures. Here, we propose a simple way to use an X-ray tomogram to infer local elastic properties. We distinguish between two scenarios of microstructure

images. In the first scenario, the material is composed by very apparent phases so the image can be easily segmented into a set of sub-spaces with homogenous properties. In the second scenario, the image, as that of sedimentary rocks, contains poorly contrasted phases, including strong intra-phase heterogeneities. For this case, we propose an alternative to segmentation techniques in order to factor in material heterogeneities. To do this, we use the local X-ray attenuation to define elastic moduli. Then, we compute up-scaled elastic moduli by solving the mechanical equilibrium. Finally, we confirm our method by comparing the up-scaled elastic moduli to indentation experiments performed at the same scale.

I. INTRODUCTION

Imaging methods are highly useful for numerical characterization as they provide the real structure of a material, while avoiding models with only partial material characteristics. However, it is technically challenging to use images as basis for simulations. Segmentation, used to determine phases, is one of the oldest, but still unsolved, challenges of image treatment [1-3]. Moreover, segmentation is often used to locate homogenous phases, which is a limitation when there are strong intra-phase variations of contrast. This article focuses on proposing a new way to use X-ray Computed Tomography (CT) for mechanical simulations, which we apply here to sedimentary rocks. This material is an emblematic material containing strong intra-phase heterogeneities, within the organic matter phase, which make it irrelevant to segment. In section II, we propose a simple linear relation between the tomography field and local elastic properties. Then, in section III, we perform a homogenization of these elastic properties by solving the

mechanical equilibrium. Finally, in section IV, we compare the resulting homogenized Young moduli to indentation performed at the same scale.

II. TOMOGRAPHY

In this section, we analyze three X-ray 3D CT images of sedimentary rocks coming from two different sites, Antrim basin (a) and Haynesville basin (b) and (c).

Rocks are cut with a low speed saw using a diamond disk of 300 μm width and then mount on sample holder fixing them with a droplet of glue. The CT scans were obtained, following the methodology [4], using a ZEISS Xradia 810 Ultra for (a) and (b) and a ZEISS UltraXRM-L200 for (c). The spatial resolution of these equipment reaches 150 μm using a Fresnel zone plate to focus the transmitted beam on a scintillator plate in front of a 20× optical device. An X-ray source (rotating anode) produces a quasi-monochromatic beam with a maximum intensity at energy of 5.4 keV for (a) and (b) and a polychromatic beam with a maximum intensity at energy of 8.048 keV from copper (Cu Kα X-ray emission) for (c). Scans were recorded with 1800 projections from -90° to 90° with an angle step of 0.1° and an exposure time of 120 s per projection for a total scanning time of 72h per acquisition including the collection of reference images. The corresponding optical magnification is 200 with a voxel size of 64 nm. The width of each sample is composed by 700 voxels, for a total volume of 45 μm^3.

Fig. 1 represents cross-sections of these three tomography images. We usually distinguish three kinds of components at this scale, minerals in dark regions, clay by shades of purple and organic matter in light colors. Details of this characterization are discussed in [5]. Note that phases of sedimentary rocks can be larger than our tomograms (> 50 μm [6,7]), and thus our CT scans are focused on specific parts enriched in organic matter. To understand our images, we

have to be aware that the image contrast, standing for the X-ray attenuation, depends on different conditions such as X-ray energy, beam intensity, sensor types and reconstruction process. That is why, in order to compare tomography images, we need to define references.

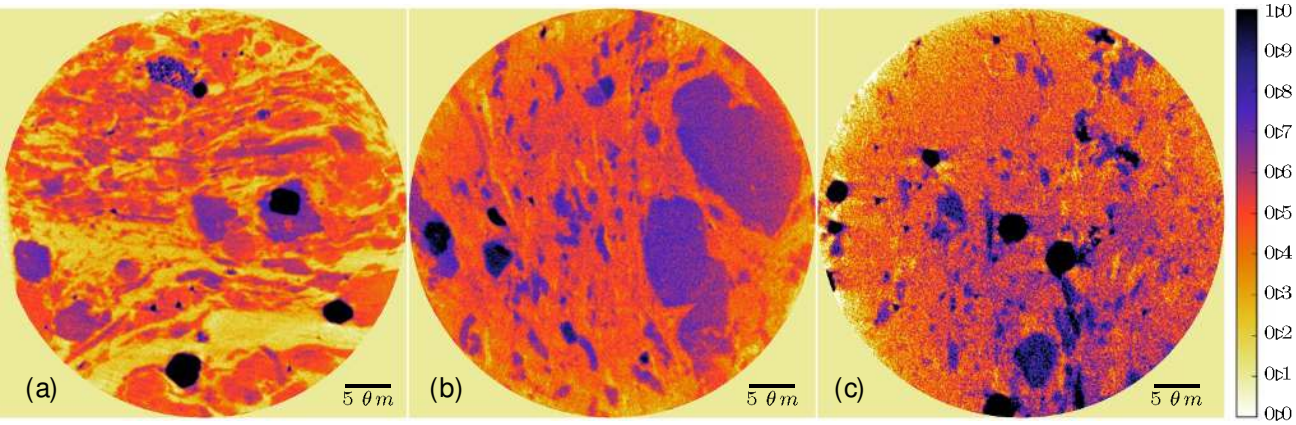

Figure 1. Cross-sections of 700×700 voxels with a resolution of 64 nm of X-ray CT scan of three samples of sedimentary rock: (a) Antrim basin, (b) and (c) Haynesville basin. (a) and (b) were obtained using a ZEISS Xradia 810 Ultra and (c) using a ZEISS UltraXRM-L200. Minerals in dark regions, clay by shades of purple and organic matter in light colors.

Fig. 2 shows the spatial distributions of X-ray attenuation for each tomogram. Each distribution has one sharp peak corresponding to the empty space surrounding the sample and one principal gaussian-like peak for the organic phase. In order to have the same references for all tomographies, we normalize the X-ray attenuation intensity with a linear function in order to obtain the same value for the empty space peak and for the main peak for all distributions. Fig. 1 and fig. 2 display X-ray attenuation intensity after this normalization step. Distributions are rescaled to have the same amplitude for the principal gaussian-like peak. In addition, there is some differences between distributions that are attributed to the geological histories and conditions of each basin. First, Antrim organic materials are mostly type II [8] while Haynesville

organic materials are type III [8], and it is well known that type II precursors contain more hydrogen and thus more aliphatic carbons, which are less dense than aromatic carbons. Second, the Haynesville basin is much deeper than the Antrim basin: 9500 ft to 16500 ft for Haynesville and 500 ft to 2000 ft for Antrim [9]. The low X-ray attenuation shoulder (around 0.25) of Antrim's distribution is attributed to both the lower basin pressure (and thus temperature) and the presence of immature organic matter that results from a higher level of hydrogen of type II precursors. Fig. 2 also exhibits a shoulder at high X-ray attenuation (around 0.7) for the Haynesville distributions, which is less present for Antrim, that can be explained by the very high pressure of the Haynesville basin.

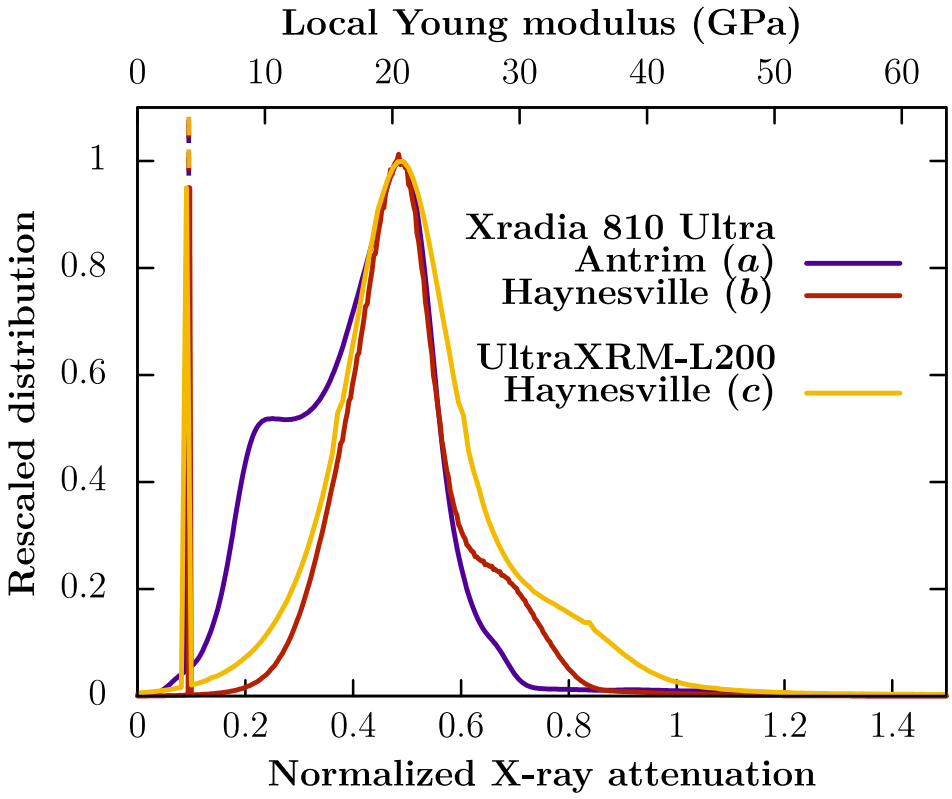

Figure 2. Rescaled distribution of normalized X-ray attenuation for the three tomographies. Peaks representing the empty space go toward the dashed lines. The upper axis is the local Young modulus assigned to the tomograms.

In order to define local elastic properties, we make two assumptions. First, the X-ray attenuation can be considered as proportional to the local density of the matter $\boldsymbol{\rho}$ [10] in case of a short X-ray path through the material (here 45 µm) and a small mass attenuation coefficient that is here not more than 10^2 cm^2/g [11]. This coefficient represents the ability of matter to absorb X-rays and depends on the energy of the photons. Second, we assume that the Young modulus increases monotonically with respect to the local density following experimental and simulated $\boldsymbol{E}$ vs $\boldsymbol{\rho}$ relation as shown by fig. 3, summarizing some typical constituents, such as nanoporous carbon [12], clay and various minerals [14,15]. Note that many mechanical engineering studies [16,17] illustrate this trend for a wide range of constituents and it is not limited to those presented in fig. 3. At first glance, we do not know which constituents are inside a tomography voxel, which is why we assume a master linear function between the Young modulus and the local density. It is important to note that since both experimental measurements and simulations in fig. 3 are from different systems and are not necessarily performed at the same scale of our voxels, this plot is likely noisier than the actual relation in our samples. Finally, these two principles lead to the simple relation that the X-ray attenuation is proportional to the Young modulus, illustrated by the top axis in fig. 2. Note that we do not attribute any rigidity to the vacuum phase since none of our simulations include a vacuum voxel. Thanks to the normalization step, we have the considerable advantage to use only one parameter to define the elastic properties of these three tomograms. We assign 20 GPa to the main peak of each distribution, which corresponds to the typical rigidity of buried organic matter [18].

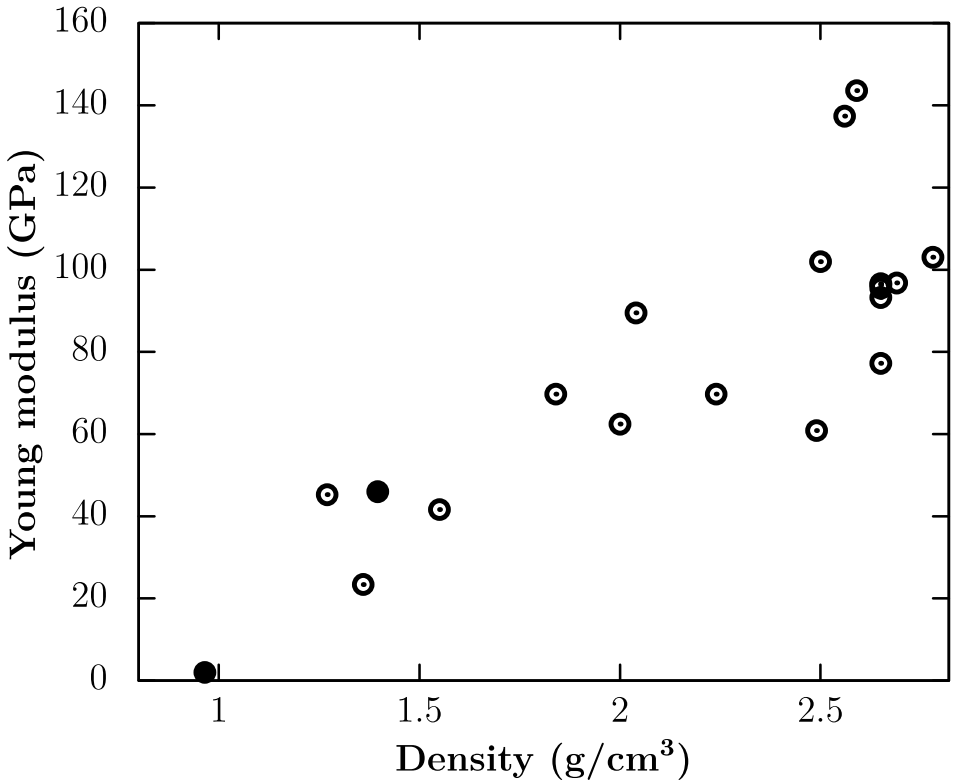

Figure 3. Young modulus function of the density for some constituents of sedimentary rock. Empty circles represent different minerals, summarized in [13] and estimated in [14,15]. Filled circles are nano-porous carbon characterization from [12].

III. HOMOGENIZATION METHOD

In this section, we homogenize, at scale $\boldsymbol{L}$, the elastic properties of sedimentary rock using our tomograms.

$\boldsymbol{L}$ defines the characteristic size of matter crushed during a micro-indentation. Here, $\boldsymbol{L}$ is about equal to 2.7 μm, equivalent to 42 voxels of our tomograms.

We first define a cube of 512^3 voxels at the center of each tomography that we then split into 512 sub-boxes of 64^3 voxels. We consider Hooke's law at any point of a sub-box, defined by $\vec{\boldsymbol{r}} = (\boldsymbol{r_1}, \boldsymbol{r_2}, \boldsymbol{r_3})$, expressed by

$$\boldsymbol{\sigma_{ij}}(\vec{\boldsymbol{r}}) = \boldsymbol{C_{ijkl}}(\vec{\boldsymbol{r}}) \cdot \boldsymbol{\varepsilon_{kl}}(\vec{\boldsymbol{r}}), \quad (1)$$

where the summation over repeated indices is assumed, $\boldsymbol{\sigma_{ij}}(\vec{\boldsymbol{r}})$ is the stress tensor, $\boldsymbol{\varepsilon_{ij}}(\vec{\boldsymbol{r}})$ is the elastic strain tensor and $\boldsymbol{C_{ijkl}}(\vec{\boldsymbol{r}})$ is the elastic stiffness tensor that we consider isotropic with a Young modulus defined by fig. 2 and a Poisson's ratio of 0.25. Fields inside a voxel are assumed homogeneous. In order to elicit the elastic response of a sub-box, we impose a small isotropic external strain $\langle \boldsymbol{\varepsilon_{ii}} \rangle_{\boldsymbol{s-box}}$. Then, we solve the mechanical equilibrium,

$$\frac{\partial \boldsymbol{\sigma_{ij}}(\vec{\boldsymbol{r}})}{\partial \boldsymbol{r_j}} = \boldsymbol{0}, \quad (2)$$

by a fixed point algorithm in Fourier space requiring periodic boundary conditions, initially proposed by [19,20] and recently improved by a variational scheme [21,22]. This fixed point converged at 10^{-7} following the criterion on $\boldsymbol{\epsilon}$ in [21] for each sub-box.

Fig. 4 illustrates, for one sub-box, the resulting elastic field for the orthogonal direction of the rock bedding (B), corresponding to the local Young modulus field (A). This field, $\boldsymbol{\varepsilon_{33}}$ exhibits the strong heterogeneities in sedimentary rocks that can go easily up to four times the amplitude of the macroscopic strain. The homogenization scale, $\boldsymbol{L}$, is smaller than the width of a sub-box in order to avoid boundary effects. Thus, we define the homogenized Young modulus $\boldsymbol{E_L}$ by averaging Hooke's law over the three directions:

$$\boldsymbol{E_L} = \sum_{\boldsymbol{i,j}} \frac{(\boldsymbol{1+\nu}) \cdot \langle \boldsymbol{\sigma_{ii}}(\vec{\boldsymbol{r}}) \rangle_{\boldsymbol{L}} - \boldsymbol{\nu} \cdot \langle \boldsymbol{\sigma_{jj}}(\vec{\boldsymbol{r}}) \rangle_{\boldsymbol{L}}}{\boldsymbol{3} \cdot \langle \boldsymbol{\sigma_{ii}}(\vec{\boldsymbol{r}}) \rangle_{\boldsymbol{L}}} \quad (3)$$

where $\langle \boldsymbol{f}(\vec{\boldsymbol{r}}) \rangle_{\boldsymbol{L}}$ is the average of a field $\boldsymbol{f}$ over the cube of $\boldsymbol{L^3}$ volume, represented by the dashed line at the center of fig. 4 (B). Note that, we consider an isotropic material at the scale $\boldsymbol{L}$ and use the same Poisson's ratio, $\boldsymbol{\nu = 0.25}$. Finally, we obtain 512 values of $\boldsymbol{E_L}$ for each tomogram.

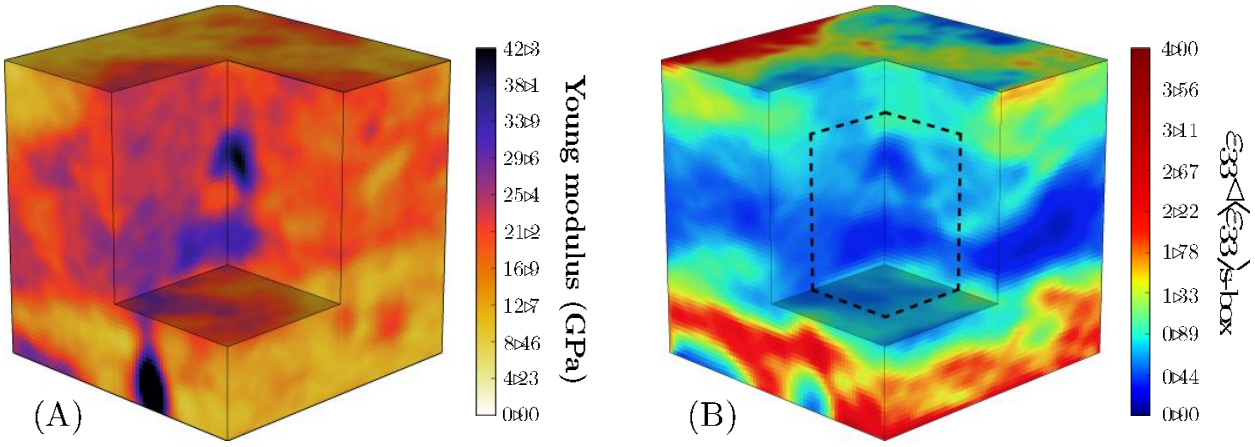

Figure 4. Simulation of elasticity of one sub-box of 64^3 voxels from Antrim tomogram: (A) Distribution of the local Young modulus following fig. 2. (B) Elastic response under an isotropic external strain. Normalized ε_{33} is displayed where r_3 is the orthogonal direction of the rock bedding. The dashed line represents the characteristic size of a micro-indentation (42^3 voxels).

IV. COMPARISON WITH MICRO-INDENTATION

In this section, we compare Young moduli ($\boldsymbol{E_L}$), obtained by simulation, to micro-indentation results.

In addition to the hardness, an indentation test provides the elasticity modulus [23,24], estimated during the unloading of the indenter and expressed, for an isotropic material, by the indentation modulus:

$$\boldsymbol{M = \frac{E_L}{1-\nu^2}}. \quad (4)$$

Multiple indentations are carried out on two samples coming from Antrim and Haynesville basins, respectively.

Fig. 5 shows, for both basins, the comparison of Young modulus distributions from micro-indentation tests (black curves) and from the simulations (color curves). Despite the noise, simulations represent quite well the shape of the experimental distributions with a maximum

around 22 GPa for both basins. Haynesville has a stronger skew toward the right. Only Antrim experiences values between 0 to 15 GPa which is consistent with the left shoulder in fig. 2 (a).

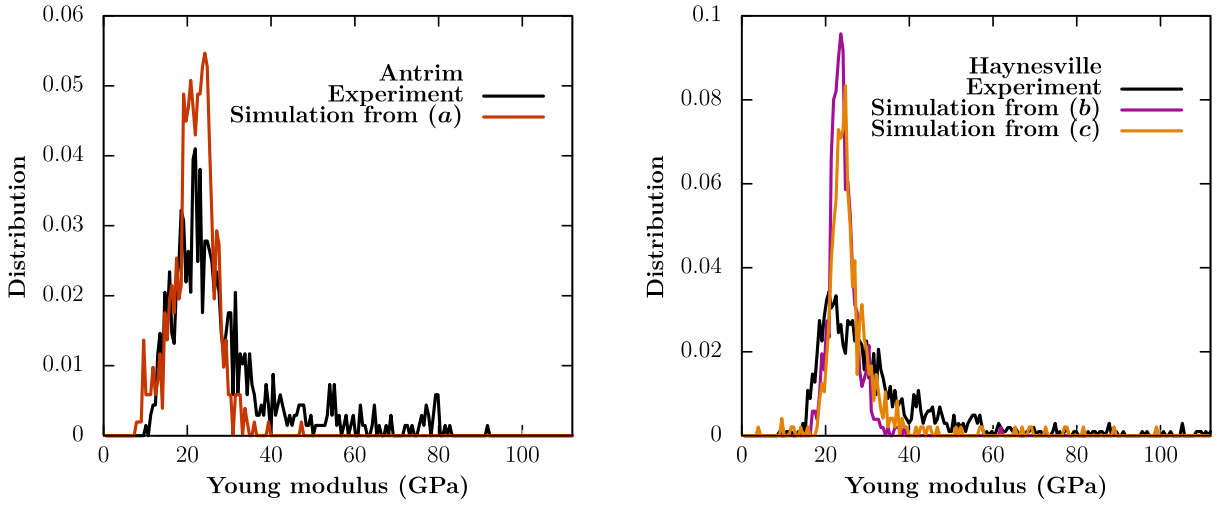

Figure 5. Distribution of Young modulus from simulations (color curves) and from experimental micro-indentations (black curves). Left: Antrim. Right: Haynesville.

V. DISCUSSION

In this study, we satisfactorily describe the elastic fields of sedimentary rocks from two different origins with only one parameter based on tomograms. The homogenized elastic properties at scale $\boldsymbol{L}$ (fig. 5) experience a peak at 22 GPa, very close to the peak of local elastic properties (fig. 2). Consequently, our samples have comparable rigidity at both scales, and do not experience the stiffening that occurs with ordered microstructures [25,26].

Also, we perceive the limit of the linear relation used to link the tomograms and the elastic properties. It describes the distribution kurtosis in fig. 5 well, but values above 40 GPa are under-represented. This means that dark phases in fig. 1 could have a higher rigidity. But the noise on both the experiments and the simulations in fig. 5 exhibits the limit of representativeness of our samples, which restricts the determination of this relation.

Another interesting point is that the distributions of X-ray attenuation are continuous (fig. 2) and so we cannot distinguish discrete densities with sharp peaks. This is consistent with the images in fig. 1 showing smooth gradient of colors besides interfaces of distinct mineral inclusions (in dark colors). Consequently, there is a large range of organic matter density. Moreover, we observe that distributions (a) and (b) in fig. 2 have the same shape of the principal gaussian-like peak. For instance, the relative difference between the two distributions in the range [0.45:0.55] of X-ray attenuation is ~1%. This means that, even though (a) and (b) come from different basins, they surprisingly have very close spectra of organic matter density. In opposition, the principal peak of (c), coming from the same basin as (b) but obtained with different acquisition conditions, is wider (relative difference rather ~10% in the range [0.45:0.55]). This is probably due to the use of a different wavelength of X-ray. This illustrates that quantitative comparisons between tomograms strictly requires the same machine conditions. Finally, we noticed the difficulties of interpreting an image due to the inherent aberration from optical systems, including defocus, tilt and chromatic aberrations. For example, we obtain voxels with a lower X-ray attenuation than in the vacuum (to the left of the sharp peak in fig. 2). As a consequence, even with high-clarity tomograms, some bias remains while using an X-ray attenuation field.

VI. CONCLUSION

Segmentation is a post-treatment commonly performed on the output of an X-ray CT scan and used to translate the image into a set of well-defined homogenous phases. We show in this study that some materials, such as sedimentary rock, experience strong heterogeneities intra-phases that are important to consider. We propose an alternative method to segmentation that

will take these heterogeneities into consideration for characterizing elastic properties. To do that, we directly link the X-ray attenuation fields to the local Young modulus using a unique parameter that we then validate with micro-indentation. We show that sedimentary rock experiences similar elastic properties at two different scales, 64 nm and 2.7 μm, respectively. Moreover, we show that, despite theirs different origins, Antrim and Haynesville rocks have similar spectra of density of organic matter. Finally, as with a regular camera, we obtain various conclusive tomograms but with different contrast and clarity depending on acquisition condition. Therefore, we propose some references to reconcile these different images.

VII. ACKNOWLEDGEMENTS

Financial support was provided by foundation AMU. The authors also thank Carl Zeiss X-ray microscopy for generously conducting the imaging work at their facilities. P.-L. Valdenaire thanks Shell Game Changer program for support.

REFERENCES CITED

[1] R. M. Haralick, L. G. Shapiro, Image Segmentation Techniques, Comput. Gr. Image Process. Vol. 29, No. 1, pp. 100-132 (1985).

[2] P. Arbelaez, M. Maire, C. Fowlkes, Contour detection and hierarchical image segmentation, J. Malik, IEEE Trans. PAMI, 33(5):898-916 (2011).

[3] L. Lalaouia, T. Mohamadib, A. Djaalab, New Method for Image Segmentation, Procedia Soc. Behav. Sci., 195 1971- 1980 (2015).

[4] N. Bossa, P. Chaurand, J. Vicente, D. Borschneck, C. Levard, O. Aguerre-Chariol, J. Rose, Micro- and nano-X-ray computed-tomography: A step forward in the characterization of the pore network of a leached cement paste, Cem. Concr. Res., 67 138-147 (2015).

[5] M. H. Hubler, J. Gelb, F.-J. Ulm, Microtexture Analysis of Gas Shale by XRM Imaging, J. Nanomech. Micromech., 7(3) (2017).

[6] M. E. Houben, G. Desbois, J. L. Urai, A comparative study of representative 2D microstructures in Shaly and Sandy facies of Opalinus Clay (Mont Terri, Switzerland) inferred form BIB-SEM and MIP methods, Mar. Petroleum Geol. Vol. 49 143-161 (2014).

[7] T. Saif, Q. Lin, B. Bijeljic, M. J. Blunt, Microstructural imaging and characterization of oil shale before and after pyrolysis, Fuel, Vol. 197 562-574 (2017).

[8] P. C. Hackley and B. J. Cardott, Application of organic petrography in North American shale petroleum systems: A review, Int. J. Coal. Geol., Vol. 163, 8-51 (June 2016).

[9] A. Agrawal, A technical and economic study of completion techniques in five emerging U.S. gas shale plays, Thesis, Texas A&M University, 2009.

[10] D. H. Phillips, J. J. Lannutti, Measuring physical density with X-ray computed tomography, NDT&E Int., Vol. 30, No. 6, pp. 339-350 (1997).

[11] N. Kucuk, Z. Tumsavas, M. Cakir, Determining photon energy absorption parameters for different soil samples, J. Radiat. Res., 54(3): 578-586 (2013).

[12] A. Obliger, P.-L. Valdenaire, N. Capit, F. J. Ulm, R. J.-M. Pellenq, J.-M. Leyssale, Poroelasticity of methane-loaded mature and immature kerogen from molecular simulations, Langmuir, 34 (45) pp 13766-13780 (2018).

[13] R. J.-M. Pellenq, N. Lequeux, H. van Damme, Engineering the bonding scheme in C-S-H: The iono-covalent framework, Cem. and Concr. Res., 38 159-174 (2008).

[14] G. Mavko, T. Mukerji, J. Dvorkin, The rock physics handbook, Cambridge University Press, second edition, 2009

[15] H. Sato, K. Ono, C.T. Johnston, A. Yamagishi, First-principles studies on the elastic constants of a 1:1 layered kaolinite mineral, Amer. Mineral, 90 1824-1826 (2005).

[16] M. Ashby, H. Shercliff, D. Cebon, Materials - Engineering, Science, Processing and Design, (University of Cambridge, third edition, 2013).

[17] M. M. Farag, Materials and Process Selection for Engineering Design, Taylor & Francis, third edition, 2014.

[18] S. Zargari, M. Prasad, K. C. Mba and E. D. Mattson, Organic maturity elastic properties, and textural characteristics of self resourcing reservoirs, Geophysics, Vol. 78, No. 4, P. D223-D235 (2013).

[19] H. Moulinec, P. Suquet, A fft-based numerical method for computing the mechanical properties of composites from images of their microstructures, IUTAM Symposium on Microstructure-Property Interactions in Composite Materials, 37:235-246, (1995).

[20] H. Moulinec, P. Suquet, A numerical method for computing the overall response of nonlinear composites with complex microstructure, Comput. Methods Appl. Mech. Eng., 157(1-2):69-94, (1998).

[21] P.-L. Valdenaire, Crystal plasticity - Transport equation and dislocation density, Ph.D. Thesis, Mines ParisTech, 2016.

[22] M. Schneider, F. Ospald, M. Kabel, Computational homogenization of elasticity on a staggered grid, J. Mech. Phys. Solids, Vol. 105, I. 9, 693-720 (2016).

[23] L. A. Galin, Contact Problems in Theory of Elasticity, translated by H. Moss, edited by I.N. Sneddon, North Carolina State College, 1961.

[24] I. N. Sneddon, The relation between load and penetration in the axi-symmetric Boussinesq problem for a punch of arbitrary profile, Int. J. Eng. Sc. 3: 47-57 (1965).

[25] H. Laubie, S. Monfareda, F. Radjaï, R. J.-M. Pellenq, F.-J. Ulm, Disorder-induced stiffness degradation of highly disordered porous materials, J. Mech. Physical. Solids, 106 207-228 (2017).

[26] H. Laubie, F. Radjai, R. Pellenq, F.-J. Ulm, Stress Transmission and Failure in Disordered Porous Media, Phys. Rev. Lett., 119, 075501 (2017).